Journal of Power Sources 196 (2011) 7076–7089

Contents lists available at ScienceDirect

Journal of Power Sources

journal homepage: www.elsevier.com/locate/jpowsour

Quantitative relationships between composition, particle size, triple phase boundary length and surface area in nickel-cermet anodes for Solid Oxide Fuel Cells

L. Holzer[a,*], B. Münch[a], B. Iwanschitz[b], M. Cantoni[c], Th. Hocker[d], Th. Graule[a]

[a] EMPA, Swiss Federal Laboratories for Materials Science and Technology, Laboratory for High Performance Ceramics, Ueberlandstrasse 129, CH-8600 Duebendorf, Switzerland
[b] Hexis Ltd., Zum Park 5, CH-8404 Winterthur, Switzerland
[c] EPFL, CIME, CH-1015 Lausanne, Switzerland
[d] ZHAW Zürich University of Applied Sciences, Institute of Computational Physics ICP, Wildbachstrasse 21, CH-8400 Winterthur, Switzerland

ARTICLE INFO

Article history:
Received 4 July 2010
Received in revised form 30 July 2010
Accepted 3 August 2010
Available online 11 August 2010

Keywords:
Microstructure
SOFC electrode
Topology
Electrochemical activity
Porous media

ABSTRACT

The present study is focusing on the elaboration of the quantitative relationships between the primary microstructural parameters (i.e. the phase volume fractions Φ, the particle and pore sizes and the corresponding size distributions PSD) with the more complex topological features (triple phase boundary length TPB_L, and specific surface area SSA) in porous Ni-cermet anodes. These relationships are crucial for the microstructure optimization and for the improvement of the corresponding electrode performance.

In the first part of the study a pristine anode material with a graded microstructure is analyzed. The results from the different zonations indicate that the TPB_L correlates well with the volume fraction of the coarsest phase which is nickel. However the volume fractions also correlate with the particle size after sintering due to stronger particle coalescence at higher nickel volume fractions. Since the larger particle size leads to a decrease of the TPB_L this coarsening effect partly neutralizes the advantage of a higher nickel volume fraction. Furthermore, the TPB_L is also linked with the nickel surface area and with the corresponding pore–nickel interface area. The pore–nickel interface is the least abundant internal surface and therefore it represents the microstructural feature which predominantly limits the TPB formation in our nickel-cermet anode.

In the second part the effects of microstructural degradation during exposure in a humid gas environment at 950 °C are investigated. During the early period (<200 h) the rapid decrease of the TPB_L is directly linked with the kinetics of nickel grain growth. At longer periods (>1000 h) the nickel coarsening ceases whereas the decrease of the TPB_L continues at a lower rate. During longer exposure time the reduction of TPB_L is most probably caused by a slight volatilization of the nickel phase and by the formation of continuous CGO layers which are shielding the surface of the nickel grains.

1. Introduction

In numerous investigations evidence was presented that the performance of composite cermet anodes (Ni/YSZ or Ni/CGO) is strongly influenced by microstructural features such as electrode composition, particle size distribution and triple phase boundary length [1–3]. However, due to methodological limitations it is still a challenging task to establish the complex relationships between these microstructural features with the electrode performance on a quantitative level. It is important to note that critical topological features such as the connectivity and the tortuosity of transport pathways in the pores can only be established based on 3D microstructural information. In this context, recent improvements in high resolution tomography using focused ion beam (FIB) [4–6] have opened new analytical possibilities and this has initiated a new field for investigations of the microstructure–performance relationships of composite SOFC electrodes [2,7–14]. In these studies the quantification of the triple phase boundary length (TPB_L) was given special attention because this is the microstructural feature where fuel oxidation (anode) and oxide reduction (cathode) take place. The triple phase boundary also represents the geometrical location, where the ion conducting ceramic phase (e.g. YSZ) converges with the electronically conductive metal phase (e.g. nickel) and with the gas transporting pores. Investigations of nickel patterned anodes give evidence that the length of the triple phase boundary (TPB_L, in $\mu m\,\mu m^{-3}$) can be directly linked with the electrode performance [15,16,35]. The same concept is also applied to porous

* Corresponding author. Tel.: +41 44 823 44 90; fax: +41 44 823 40 23.
E-mail address: lorenz.holzer@empa.ch (L. Holzer).

0378-7753/$ – see front matter © 2010 Elsevier B.V. All rights reserved.
doi:10.1016/j.jpowsour.2010.08.006

cermet anodes, where the TPB-line is extended into the electrode microstructure.

At a closer look, one has to take into account that the reaction mechanism of fuel oxidation includes many different reaction steps [17,36] whereby three different groups can be distinguished: (a) nickel surface reactions, e.g. adsorption and dissociation of the fuel on the nickel surface; (b) ceramic surface reactions, e.g. the formation of hydroxides on the surface of YSZ; and (c) charge transfer reactions. Many of the reaction steps can take place at a certain distance away from the TPB and thus these reaction steps are not strictly bound to the TPB. As a first approximation, however, the TPB can be interpreted as the geometrical feature of the composite electrode where the bulk electrochemical reaction of the electrode takes place.

Furthermore it is also important to note, that the TPB is only active in the case where all three phases are connected with their respective base. For example the pores must form a percolating network which is linked with the gas channel. In a similar way the nickel phase must be connected with the metallic inter-connector and the ceramic phase with the electrolyte. When optimizing anode microstructures for improved electrode performance, it is thus not sufficient to maximize the total TPB_L. The connectivity-aspects must be taken into account in order to ensure electrochemical activity at the TPB.

In the mentioned studies based on FIB-nanotomography it was possible for the first time to distinguish between active and inactive components of the TPB_L by taking into account the percolation of all three phases. For example active TPB-lengths of 3.7 and 4.9 $\mu m\,\mu m^{-3}$ were found to represent 88 and 67% of the total TPB_L [8] in Ni–YSZ anodes. In another FIB-study of a coarser grained Ni–YSZ anode [10] smaller values were found for the active TPB_L (1.0–1.7 $\mu m\,\mu m^{-3}$) which represented only 40–65% of the total TPB_L.

Nevertheless, the TPB is not the only microstructural parameter which is important for the electrode performance. For the microstructural optimization two groups of parameters can be distinguished. The so-called 'second order topological parameters' which include TPB_L, connectivity, catalytic surface area and tortuosity have a direct impact on the electrochemical activity and/or on the associated transport properties. Unfortunately these parameters are difficult to control during the electrode production. In contrast, the first order parameters which include electrode composition (i.e. volume fractions Φ_{pore}, Φ_{el}, Φ_{ion}) and particle sizes ($r_{50,pore}$, $r_{50,el}$ and $r_{50,ion}$) are usually much easier to control. A systemic understanding of the relationships between the 'tunable' first order parameters with the 'performance relevant' second order parameters could thus enable a more purposeful microstructure optimization.

Hence, 3D-analysis with FIB-tomography seems to be the favored method for a systematic investigation of these relationships. However, since this method is very time consuming its suitability for parametric studies with a large number of samples with different compositions is limited. As an alternative approach simulation of virtual microstructures can be used to quantify the different geometrical parameters and their interdependencies. Microstructural modeling is particularly suitable for extensive parametric studies. For example, virtual microstructures of composite Ni/YSZ anodes have been modeled with spherical particles of ionic and electronic conductors [18–21]. The results indicate that the TPB_L can be strongly increased when the particle sizes are reduced. In addition, the results from microstructure simulation also indicate that the ideal composition for the maximum TPB_L is depending on the size ratio of the solid components. For equal particle sizes of the electronic and ionic conducting phases ($r_{50,el}/r_{50,ion} = 1$) the maximum TPB_L is obtained for a composition with equal amounts of both solid components (i.e. $\Phi_{el} = \Phi_{ion} = 0.5$, whereby $\Phi_{el} = V_{el}/(V_{el} + V_{ion})$). Furthermore the results from microstructural modeling also predict a significant decrease of the active TPB_L for compositions below the percolation threshold [19,21] which is in the following range of volume fractions: Φ_{ion} or $\Phi_{el} = 0.2–0.35$.

At the present stage, the virtual microstructures from modeling are usually assuming idealized, isotropic and uniform geometries with simple particle shapes and with a random spatial distribution of the particles [22]. However, the microstructures of real composite anodes are strongly disordered and the particles tend to have complex (non-spherical) shapes. In addition effects of agglomeration in the initial pastes and microstructural reorganization during sintering and degradation may lead to non-random spatial distributions. For example in real microstructures continuous CGO layers may form during degradation on the surface of the coarse nickel particles due to the 'wetting' behavior of the ceramic phase. The virtual reconstruction of such disordered microstructures is difficult to achieve by means of numerical and geometrical models. Consequently an experimental validation of the modeled microstructures is required which can be done with FIB-tomography.

The aim of this study is thus to establish quantitative relationships between primary microstructural parameters that can be adjusted during materials processing with the higher order topological parameters that control the electrochemical performance of the anode. For this purpose we are applying FIB-nanotomography together with advanced image analysis tools for a thorough quantitative description of the microstructures in porous nickel/CGO anodes. The screen printed anode material consists of a graded microstructure which includes four distinct zones with different compositions and with different particle size distributions (see Fig. 2). Based on the gradual changes in the four zones the basic microstructural relationships between primary parameters and higher order topology shall be elaborated. The parameters under investigation are the phase contents (Φ_{pore}, Φ_{el} and Φ_{ion}), the particle and pore sizes ($r_{50,pore}$, $r_{50,el}$ and $r_{50,ion}$) and the corresponding particle size distributions (discrete PSD_D and continuous PSD_C), the particle number densities (N_V), the degree of percolation, the TPB_L, the specific surface area (SSA) of each phase and the specific interfacial area (SIA) between the different phases.

In addition we are applying the same techniques for the quantitative investigation of microstructural changes that occur during anode degradation. In a separate study [23] the same bi-layer anode material was exposed to different gas compositions at 950 °C. Thereby the kinetics of nickel grain growth was quantitatively described for periods up to 2300 h [24]. In the present study we are now extending this investigation on anode degradation by analyzing the corresponding changes of the TPB_L and of the specific surface areas (SSA) and interfaces (SIA). Thereby a correlation between the grain growth of nickel with the contemporaneous decrease of the TPB_L shall be established. This correlation gives new insight to the basic mechanisms of anode degradation on a microstructural level.

Finally, the measured pairs of TPB_L with the corresponding anode compositions from pristine and degraded anodes are compared with similar data sets from literature that were obtained by means of microstructural modeling (see Fig. 18). This comparison enables the identification of compatible trends in real samples and in simulations. These findings are considered as a basis for the future microstructure optimization of high performance anodes.

2. Materials, experiments and methodologies

2.1. Fabrication of anode with graded microstructure

Ni/CGO anode powders from Praxair Specialty Ceramics were mixed with a terpineol based solution in a ball mill. The pastes

Table 1
Microstructural information related to the data points in Fig. 18 where TPB-Lengths are plotted as a function of composition.

Data points in Fig. 18	Literature/reference	Particle radii (discrete PSD) of electronic (Ni) and ionic (CGO/YSZ) conducting phases	Ratio of particle radii from el. and ionic cond. phases	Porosity
Nr 1–3: TPB-data from numerical modeling/virtual anode microstructures from literature				
Nr 1:	Kenney et al. [20]:	$r_{el} = r_{ion} = 250$ nm	$r_{el}/r_{ion} = 1.0$	$\Phi_{pore} = 0.3$
Nr 2:	Abbaspour et al. [19]:	$r_{el} = r_{ion} = 500$ nm	$r_{el}/r_{ion} = 1.0$	$\Phi_{pore} = 0.3$
Nr 3:	Abbaspour et al. [19]:	$r_{el} = 1000$ nm/$r_{ion} = 500$ nm	$r_{el}/r_{ion} = 2.0$	$\Phi_{pore} = 0.3$
Nr 4–6: TPB-data from real anode materials/analyzed in this study				
Nr 4:	This study, graded anode with 4 zones (see Fig. 2)	ZII: $^*r_{el} = 1240$ nm/$^*r_{ion} = 400$ nm	$r_{el}/r_{ion} = 3.0^*$	$\Phi_{pore} = 0.35$
		ZIII: $^*r_{el} = 1110$ nm/$^*r_{ion} = 440$ nm	$r_{el}/r_{ion} = 2.5^*$	$\Phi_{pore} = 0.35$
		ZIV: $^*r_{el} = 910$ nm/$^*r_{ion} = 540$ nm	$r_{el}/r_{ion} = 1.7^*$	$\Phi_{pore} = 0.34$
		ZV: $^*r_{el} = 1010$ nm/$^*r_{ion} = 710$ nm	$r_{el}/r_{ion} = 1.4^*$	$\Phi_{pore} = 0.20$
Nr 5:	Holzer et al. [24], anode layer 1 (Fig. 15): degradation in a humid forming gas at 950 °C			
Nr 6:	Holzer et al. [24], anode layer 2 (Fig. 15): degradation in a humid forming gas at 950 °C			

Note: $^*r_{el}$ and $^*r_{ion}$ are obtained from continuous PSDs (R_{50}) by multiplication with a proportionality factor of 2.8 which relates continuous with discrete particle sizes (see Fig. 11).

are composed of 50 wt% NiO and 50 wt% CGO (anode layer 1) and of 70 wt% NiO and 30 wt% CGO (anode layer 2). The slurries were screen printed in two layers on a 3YSZ electrolyte (Nippon Shokubai). Anode layer 1 is facing the electrolyte, whereas anode layer 2 is a current collecting layer on top of it. The anodes were sintered at 1350 °C for 4 h. During sintering distinct interface layers formed between anode layers 1 and 2 and between electrolyte and anode layer 1. These interface layers have compositions that are different from the neighbouring anode layers 1 and 2. In this way a graded microstructure was obtained and four different zones are distinguished in the 3D-analysis with FIB-tomography (see Fig. 2).

2.2. Degradation experiment

In a previous study on anode degradation, nickel grain growth was quantified from Ni/CGO samples that were exposed to dry and to humid conditions at 950 °C [23,24]. The samples were produced in a similar way as described above in chapter 2.1. In the previous investigation first order microstructural parameters (volume fractions, size distributions) were quantified for 8 time steps between 0 and 2286 h exposure time. In the present study we use the 2D image data that was acquired by SEM from samples that were exposed in humid gas at 950 °C and we extended the microstructural analysis with second order parameters (TPB and surface area).

The degradation experiment was performed in a tube furnace inside an aluminium-oxide tube. Small pieces of the anode/electrolyte half cells (~0.25 cm^2) were placed on an aluminium-oxide sample holder. The temperature was measured directly on the sample holder using a type S thermocouple. A Pt/YSZ/Pt sensor was used to measure the Nernst-potential. Hydrogen and nitrogen were mixed with mass flow controllers and a precision evaporator from Bronkhorst (Controlled Evaporator Mixer) was used to humidify the gas. The furnace was heated up and cooled down with a rate of 3 °C min^{-1}. For the first reduction the samples were heated to the reduction temperature (950 °C) in oxidizing atmosphere. Afterwards the tube was flushed with N_2 for 2 h followed by the introduction of hydrogen for reduction. The reduction at 950 °C was considered to be completed after 1 h of hydrogen flow which is considered to be the initial data point at 0 h. During the degradation experiment the gas mixture consisted of forming gas and additional water vapour (Nernst-potential: 0.87 V). Single pieces of the anode/electrolyte half cells were removed at different exposure times from the furnace. For this purpose the furnace was cooled down and reheated under reducing atmosphere. The maximum exposure time was 2300 h.

2.3. Microstructure analysis

The quantitative microstructure analysis includes sample preparation, image acquisition by SEM or FIB, segmentation and 3D-reconstruction (only for the FIB-data), and quantification of first and second order parameters. All these procedures have been described in previous publications and here we only present a short description.

2.3.1. Sample preparation and image acquisition

All samples for microstructure investigation are produced by infiltrating the pores with a resin (4 parts Araldite BY158 mixed with 1 part Aradur hardener) followed by grinding, polishing and finally coating with a thin carbon layer. 2D-imaging is performed with a FEI Nova NanoSEM230. BSE images are captured with a conventional solid state detector at 5 kV and spot 4. FIB-nanotomography is performed with a Zeiss NVision at EPFL. During serial sectioning, a sequence of electron images is obtained at 2 kV by using the ESB-detector. The FIB-milling is performed with an ion-beam current of 3 nA at 30 kV. More details about FIB-nanotomography and 3D-reconstruction are presented in dedicated articles [4–6,25].

2.3.2. Segmentation and 3D-reconstruction

A special segmentation procedure was developed for precise and reproducible phase recognition in composite electrodes [24]. This segmentation procedure is applicable to 2D data from SEM and to 3D data from FIB. In the same study also a parametric study was performed in order to determine the image window size which is necessary for representative quantitative analysis and the pixel resolution which is necessary for reproducible particle size measurements from the Ni/CGO anodes. It was found that images with an area of 400 μm^2 will give representative quantitative analyses and pixel resolutions better than 35 nm are sufficient for reproducible particles size measurements. In the present study the FIB-tomography data is acquired at 12 nm voxel resolution and the SEM images at 15–25 nm pixel size. All analyses in the present study are based on image windows larger than 400 μm^2 and hence, representative and reproducible results may be expected.

2.3.3. First order microstructural parameters: discrete and continuous PSD analysis

The first order parameters include volume fractions, particle and pore size distributions (PSDs) and average particle radius (R_{50}). Volume fractions can be determined with standard procedures. In contrast PSD analysis deserves special consideration. A major prob-

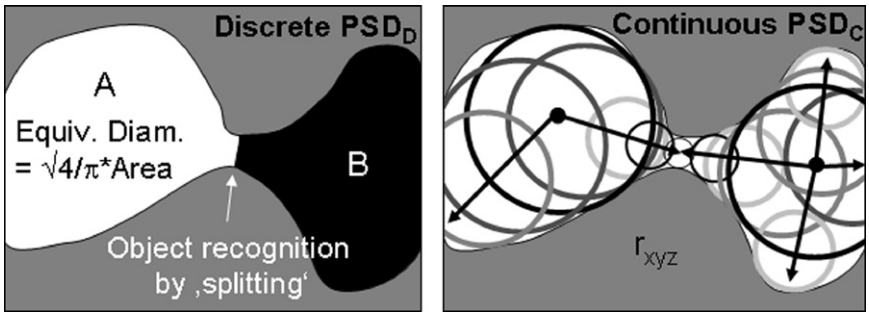

Fig. 1. Illustration of geometrical principles which are inherent to two different types of particle size distributions (PSDs) modified after [24]. Both PSD methods are based on a different definition for 'object size'. *Left: discrete PSD$_D$*: The particle size is defined as area (2D) or volume (3D) equivalent diameter. *Note*: Networked microstructures have to be split into discrete objects by splitting [26]. *Right: the continuous PSD$_C$* [29] is based on an algorithm which measures the area (2D) or volume (3D) that can be occupied with a circle or sphere of a given radius. By incrementally reducing the radius increasingly larger areas (volumes) can be occupied. In this sense the continuous PSD measurement also represents the simulation of a pressure induced intrusion with a poorly wetting fluid (similar to the mercury intrusion porosimetry).

lem for PSD analysis based on imaging techniques is the fact, that the primary particles (i.e. the initial grains of NiO and of ceramic powder) undergo coalescence during reduction and sintering at high temperatures. The sintering process thus results in percolating networks with complex shapes. After sintering it is therefore very difficult to identify the boundaries of the individual grains. The question then arises, what is a 'discrete particle object' and how do we define 'particle size'? In this context it is important to note that different geometrical concepts have been developed for the measurement of particle size distributions, which will be discussed in the following sections.

The discrete particle size distribution (PSD_D) (Fig. 1, left) is based on the recognition of individual objects such as the primary particles. For the recognition of distinct objects from a continuous network, the percolating chains have to be split into smaller segments representing discrete particles. For this purpose a specific splitting algorithm was developed which is capable to identify concavities that are interpreted as 'necks' between the discrete particles [26]. The continuous network is split along these necks into discrete particles. However the curvature of the concave necks may be strongly variable. Therefore, the degree of splitting can be adjusted with the so-called *k*-parameter. In a parametric study the correct degree of splitting was evaluated by applying 11 *k*-parameters between 0.0 and 1.0 for the analysis of a 3D microstructure representing a densely packed cement powder. The PSD-analyses of the resulting particle structures revealed that the splitting with a *k*-value of 0.6 produces a realistic granular texture from the percolating network [27]. It is important to note that the discrete method is not suitable for 2D analysis, but it is only reliable when using it in combination with high resolution 3D-microscopy [28]. Furthermore, the determination of discrete PSD_D also requires the correction of the boundary truncation effects which is described elsewhere [26]. Although the discrete PSD measurement is challenging and time consuming, this method is important, since most experimental techniques (light scattering, laser granulometry) and also the geometrical modeling are based on the same concept which includes the perception of discrete objects (e.g. primary particles).

In contrast, the continuous particle size distribution (PSD_C) is based on a geometrical simulation whereby a percolating network is filled with spheres (circles in 2D) of a given radius. By reducing the radius of the spheres incrementally, more constricted locations such as the bottle necks can be filled. The cumulative PSD is then obtained by relating the incrementally filled volume (area in 2D) with the corresponding radii. A thorough description of the continuous PSD method is given elsewhere [29]. It is an important advantage of this method that it can be applied to percolating networks without any preceding splitting and without the challenging recognition of discrete particles. Furthermore, the application of the continuous method to 2D images results in nearly identical PSD curves as obtained from 3D-images of the same material [30].

In the present study we will apply both methodologies, discrete and continuous PSD. Since both methods are based on very different geometrical concepts also very different results are expected. Thereby, the discrete PSD_D can be correlated with the results from microstructural modeling, which is based on similar geometrical concepts. However, since the discrete method is very time consuming, only a limited number of 3D-cubes from FIB-nanotomography are analyzed in this way. In contrast the continuous PSD_C can be used for a larger amount of samples which are mainly investigated in 2D. This continuous method thus opens new possibilities to study efficiently the time resolved changes which occur during anode degradation and associated grain growth.

2.3.4. Second order microstructural parameters: TPB_L and surface areas

The second order parameters investigated in this study include triple phase boundary length (TPB_L), specific surface areas (SSA) of pore, nickel and CGO and the specific interface areas (SIA) of pore–nickel, pore–CGO and nickel–CGO.

In this study the TPB_L is determined with the so-called centroid method, in analogy to the procedure described by Iwai et al. [10]. The total triple phase boundary can be measured either from 2D images or from 3D tomographs. However, the measurement of the active TPB_L requires information on the connectivity of each phase, which can only be obtained from 3D-analysis.

The total TPB_L is determined by identifying all pixels (in 2D) and all voxels (in 3D) that have common edges of faces with the other two phases. In 2D the total TPB_L represents geometrical points and it is calculated by normalizing the number of single TPB objects to the image area [$-/\mu m^2$]. In our 2D analyses each TPB object includes 4.8–5.0 pixels. Alternatively, when calculating the TPB_L from 3D data, then each TPB object represents a line and the TPB_L is the sum of these lines normalized to the image volume [$-/\mu m^2$]. Theoretically the values of the total TPB_L are identical in 2D and in 3D analyses, under the condition that the investigated microstructures are isotropic and that the correct stereological correction is applied. According to [34,31] a factor of 2 has to be introduced for the 2D analyses of TPB because the length in a volume (*LV*) is equal to twice the number of points in a surface (*PA*), $LV = 2PA$.

In samples with isolated particles the active TPB is always smaller than the total TPB. As discussed by Wilson et al. [7,8] 3D information is necessary for the distinction between active and inactive TPB components. In the present study the 3D-connectivity analysis which is based on FIB-tomography data and on discrete object recognition before splitting is performed only on the pristine Ni/CGO sample whereas the TPB analysis in the degradation

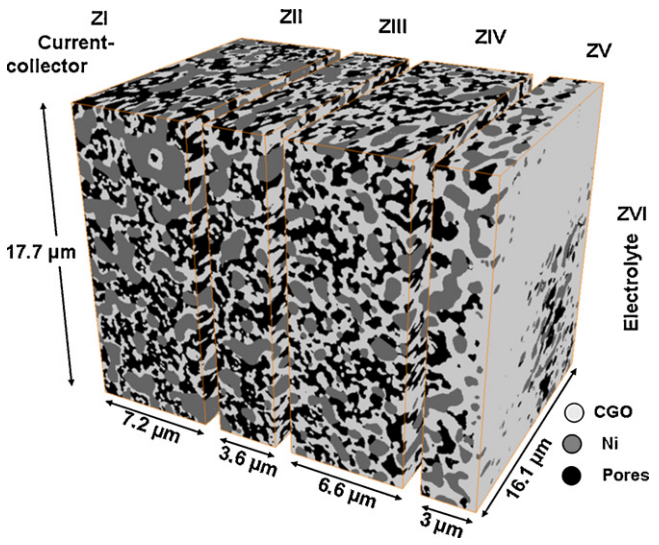

Fig. 2. 3D-reconstruction of porous Ni/CGO anode from FIB-nanotomography. The graded microstructure consists of four different zones (ZII to ZV) which are analyzed separately. The data volume has dimensions of 20.4 µm × 17.7 µm × 16.1 µm (=5.84 × 10^3 µm^3). The volume consists of 1701 × 1477 × 1345 voxels (=3.38 × 10^9). The voxel size ('resolution') is 12 nm × 12 nm × 12 nm.

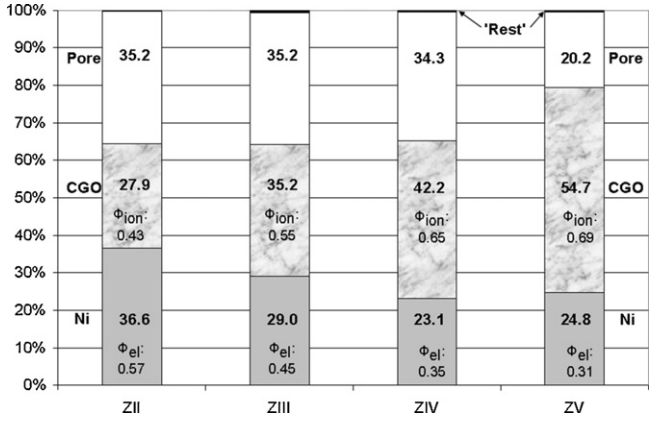

Fig. 3. Phase compositions of four zones in the graded Ni/CGO anode, measured from the FIB-data cube shown in Fig. 2. The solid volume fraction of Ni (Φ_{el} = Ni/(Ni + CGO)) is decreasing from ZII (contact with metallic inter-connector) to ZV (interface anode–electrolyte). At the same time the solid volume fraction of CGO is increasing towards the electrolyte (Φ_{ion} = CGO/(Ni + CGO)).

experiment is based only on 2D SEM imaging. The 3D-connectivity analysis indicates that all three phases in the pristine Ni/CGO sample form nearly perfectly percolating networks (more than 99% connectivity) which means that nearly the total TPB_L is active in this sample. However, for the TPB analyses from the degradation experiment which are performed only in 2D, the effect of potentially isolated, non-connected particles on the TPB activity cannot be determined. The possible limitations of 2D analyses for TPB measurements will be further discussed in Section 3.2.

For the measurement of surface and interface areas the voxel (3D) or pixel (2D) based images are transformed into triangulated (3D) or vectorized (2D) images after segmentation. For each phase and for each type of interface the measured surface areas are then normalized to the image window size (3D: [µm^2 µm^{-3}], 2D: [µm µm^{-2}]).

3. Results and discussion

3.1. 3D-analysis of a composite Ni-CGO anode with graded microstructure

3.1.1. Anode compositions of zones ZII to ZV

A 3D-reconstruction based on FIB-tomography of the graded anode microstructure is shown in Fig. 2. The FIB-data with a volume of 20.4 µm × 17.7 µm × 16.1 µm (=5.84 × 10^3 µm^3) represents a cross-section of the entire anode which was screen printed in two layers. After thermal treatment distinct transition zones have formed at the interfaces of the two anode layers. Five zones can therefore be distinguished (from left to right): ZI: interface between metallic inter-connector and anode layer 2 (not shown). ZII: anode layer 2, which is a functional layer for current collection and for gas distribution. ZIII: interface between anode layers 1 and 2. ZIV: anode layer 1, which is the electrochemically active layer. ZV: interface between anode layer 1 and solid electrolyte (also active). In the following sections the microstructures of zones ZII to ZV are analyzed separately.

The compositional variations of these four zones are illustrated in Fig. 3. The porosity (Φ_{pore}) is constant at 35 vol.% from ZII to ZIV but it is reduced to 20 vol.% in ZV. The pore volume fraction of 35% is considered to be sufficient for gas diffusion under current load. In contrast to the porosity the solid volume fractions are changing gradually. Thereby the amount of the nickel phase (Φ_{el} = solid volume fraction of electronically conducting phase = $V_{Ni}/(V_{Ni} + V_{CGO})$) is increasing from 0.31 in ZV to 0.57 in ZII in order to ensure electronic conduction in the vicinity of the metallic inter-connector. In a complementary way the volume fraction of CGO (Φ_{ion} = solid volume fraction of ionic conducting phase) is increasing towards ZV, so that it guarantees for a percolating network of the ionic conducting phase at the interface with the electrolyte.

3.1.2. Discrete particle size distributions (PSD_D)

Particle size analysis is strongly depending on reliable object recognition. For the determination of discrete PSDs the continuously networked, percolating phases have to be split into discrete objects. For this purpose a special algorithm was developed [26]. The effect of splitting with increasing k-values is investigated in the following section for the anode microstructure in zone ZII.

Fig. 4 illustrates the particle structures of Ni in ZII. After segmentation of the nickel phase (gray pixels in the left cube) and after splitting with increasing k-values (0.0, 0.6 and 1.0), each discrete particle object is labeled with a specific color. This results in three cubes with different particle structures of the nickel phase. For k = 0 (2nd cube from left, i.e. no splitting) the majority of the nickel phase still has the same color which indicates that nickel in zone ZII forms a perfectly percolating network. Only a few colored grains at the surface are apparently disconnected from the main nickel network. As discussed by Wilson et al. [8] such small particle islands at the cube surface most probably represent artifacts related to boundary truncation effects, but probably not really disconnected particles.

Due to the splitting with k = 0.6 (2nd cube from right) and with k = 1.0 (right cube) the microstructure becomes more and more fragmented. A parametric study for splitting of densely packed cement powder was performed previously which indicated that splitting with k = 0.6 results in a realistic recognition of the particle objects [27]. In the present study we therefore consider k = 0.6 as the most reasonable degree of splitting.

The discrete particle size distributions (PSD_D) of nickel in the three split cubes are measured both, in relation to the volume fractions (V_V) and in relation to the particle number densities (N_V). In the volumetric PSD curve for the non-split nickel structure (V_V k = 0.0) a significant step is observed at an apparent particle diameter of about 70 µm which has no physical meaning. This step represents 99 vol.% of the total nickel volume which indicates that nickel in ZII forms a nearly perfectly percolating network. With

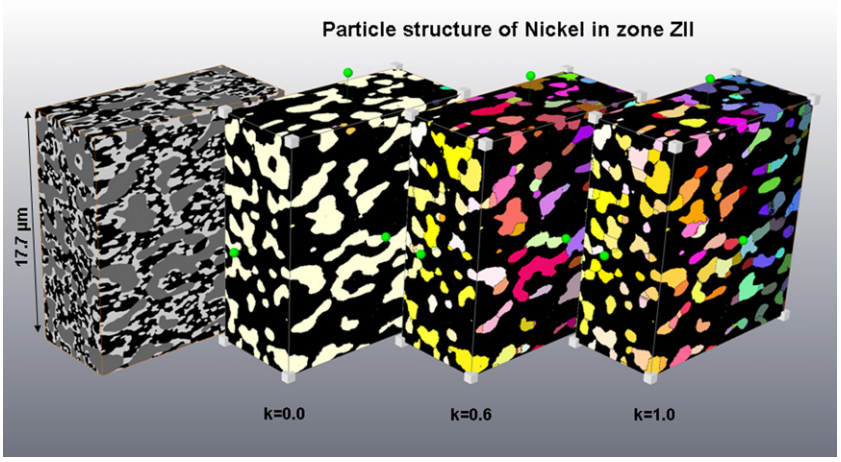

Fig. 4. Object recognition of discrete nickel particles in zone ZII based on a splitting algorithm which is capable to identify concave geometries (necks) [26]. After splitting each discrete object is labeled with a different color. *Left cube*: 3D-reconstruction of microstructure in zone ZII from FIB-nanotomography with nickel (gray), CGO (white) and pores (black). *2nd cube from left* ($k = 0.0$), *2nd cube from right* ($k = 0.6$) and *right cube* ($k = 1.0$) represent the color labeled particle structures of nickel after splitting with increasing k-values. *Note*: A parametric study has shown that splitting with $k = 0.6$ results in realistic particle structures [27]. The cube resulting from $k = 0.0$ can be used to identify the percolating components and the disconnected particles of the initial particle structure before splitting. $k = 1.0$ represents the particle structure at the maximum degree of splitting. The discrete PSD_D-curves corresponding to the microstructures of the three labeled cubes are shown in Fig. 5.

increasing splitting the nickel network is then virtually fragmented into discrete particles. In the microstructure which is split with $k = 0.6$ the particle diameter D_{50} is reduced to 2.4 µm (V_V $k = 0.6$). It has to be mentioned that k-values of 0.5 or of 0.7 produce nearly identical PSD curves. Even at the maximum degree of splitting ($k = 1.0$) the difference to $k = 0.6$ is only moderate and the D_{50} is 2.2 µm.

When looking at the PSD curve related to the particle number density of the non-split nickel structure (N_V $k = 0.0$) it becomes obvious that the majority of the discrete objects have diameters below 100 nm. It is important to note that the corresponding volume of these small particles is less than 1% (see V_V $k = 0.0$, for diameter < 0.1 µm). These apparently disconnected particles may thus not strongly affect the overall electrochemical performance due to the small volume they are representing. In addition, many of these small particle islands are located at the cube boundary and their disconnection may represent artifacts from boundary truncation (as discussed above).

In a similar way as it was shown in the previous sections for the nickel phase, also the CGO and the pore phases are split into discrete objects then color labeled (see Figs. 6 and 8) and then analyzed for the discrete particle size distributions (Figs. 7 and 9). For both the CGO and the pores the PSDs before splitting (V_V $k = 0.0$) reveal step functions, similar as for the nickel. Hence also the CGO and the pore phase in zone ZII form a percolating network which includes more than 99% of the phase volume. When comparing the PSDs of Ni and CGO it becomes obvious that CGO not only has the smaller particle sizes but the splitting also leads to a much higher amount of discrete particles (see e.g. PSD curves 'Nv $k = 0.6$' related to particle nr densities in Fig. 5 and in Fig. 7). Qualitatively it is also important to note, that the CGO particles are not randomly distributed in space but they tend to cover the surface of the larger nickel grains.

3.1.3. *Continuous particle size distributions (PSD_C) and comparison with discrete PSD_D*

The measurement for discrete particle size distributions is a time consuming procedure which includes many processing steps such as splitting, labeling and correction of boundary truncation. Since discrete PSD_D gives reliable results only for the case where it is applied to relatively large 3D data cubes this method also requires

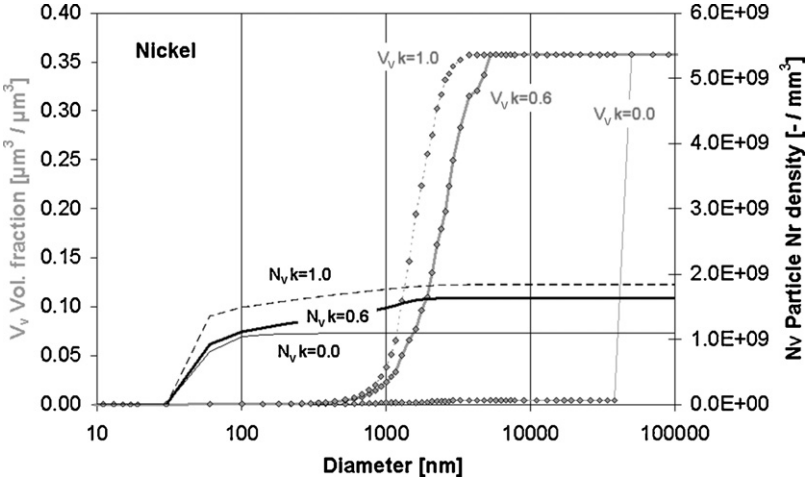

Fig. 5. Cumulative curves of discrete particle size distributions (PSD_D) for nickel in zone ZII, before splitting ($k = 0$), after 'realistic' splitting ($k = 0.6$) and with maximum splitting ($k = 1.0$). V_V denotes cumulative PSD curves related to the volume fraction. *Note*: For $k = 0$ a step function is obtained, which indicates that 99 vol% of the nickel forms a single percolating network. With increasing k-values this network becomes fragmented which leads to smaller mean particle sizes. N_V denotes the cumulative PSDs related to the particle number density. *Note*: More than 90% of all particles are smaller than 100 nm (N_V), however the corresponding volume of these small particles is less than 1 vol% (V_V).

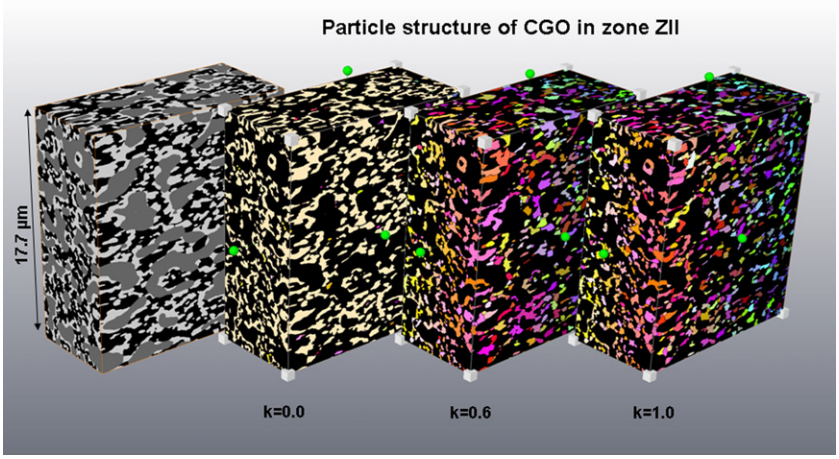

Fig. 6. Object recognition of discrete CGO particles in zone II based on splitting and color labeling. *Left cube*: 3D-reconstruction of microstructure in zone ZII from FIB-tomography with nickel (gray), CGO (white) and pores (black). *2nd cube from left* ($k = 0.0$), *2nd cube from right* ($k = 0.6$) and *right cube* ($k = 1.0$) represent the color labeled particle structures of CGO after splitting with increasing k-values. The corresponding PSD curves are shown in Fig. 7.

significant computing capacities. As an alternative technique a so-called 'continuous PSD_C' method was developed, which is capable to determine size distributions from networked microstructures without identification of discrete objects [29]. This method also works well when it is applied to 2D images. The continuous PSD_C curves for all three phases (nickel, CGO and pores) and for all four zones (ZII to ZV) in our 3D data from FIB-tomography are plotted in Fig. 10. From each PSD curve the total volume fraction (maximum of cumulative PSD curve) and the 'average radius' (r_{50} = radius corresponding to 50% of maximum PSD-volume) can be obtained. Fig. 10 illustrates that the compositional change in the graded anode microstructure is associated with a systematic change of the average particle and pore sizes. For example the gradually increasing nickel contents from zone ZV (25 vol.%) to zone ZII (37 vol.%) are associated with an increase of the 'average radius' (r_{50}) from 324 to 444 nm. In a similar way also the gradual increase of the CGO contents from zone ZII (28%) to ZV (55%) is associated with an increase of the average particle size of CGO (from 144 to 252 nm). In contrast the average pore size (ca. 190 nm) and the porosity (ca. 35%) remain constant in zones ZII to ZIV. In zone V the pore volume is reduced (20%) but the pore size is slightly larger (204 nm) compared to the other three zones.

It has to be mentioned that the continuous PSD_C method is based on a very different geometrical concepts than the discrete PSD_D and therefore the measured object sizes can be very different (especially for complex particle shapes). This is illustrated in Fig. 11 which summarizes the average radii (r_{50}) from discrete and continuous PSD measurement of nickel, CGO and pores in zone ZII. Thereby the ratio of discrete over continuous radii (r_{50}) is 2.8 ($\pm$0.1) for all three phases. In the present paper we are thus using this ratio of 2.8 as a proportionality factor that relates the results from discrete and continuous PSD methods. In this way, it can be used for the comparison of discrete PSDs from microstructural models (in literature) with the continuous PSDs which are easier and faster to be measured from the real microstructures (networked, percolating) after thermal treatment (sintering and reduction). For example it was shown that continuous PSD measurements give nearly identical results for both 2D and 3D image data which were acquired from same material [30]. This opens new possibilities for efficient quantification of particle structures in a series of samples, which was

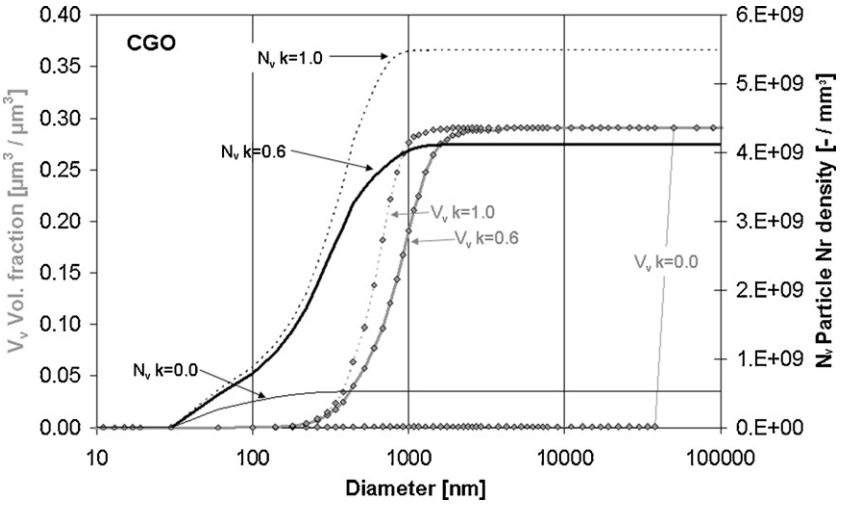

Fig. 7. Cumulative curves of discrete particle size distributions (PSD_D) for CGO in zone ZII, before splitting ($k = 0$), after 'realistic' splitting ($k = 0.6$) and with maximum splitting ($k = 1.0$). Vv denotes cumulative PSD curves related to the volume fraction. Nv denotes the cumulative PSDs related to the particle number density. The splitting leads to a much higher particle density of CGO compared to nickel (see Fig. 5).

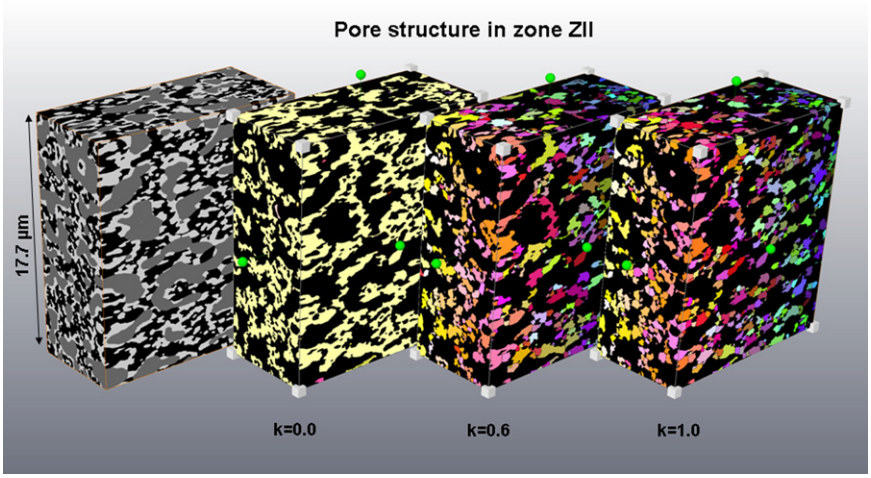

Fig. 8. Object recognition of discrete pore objects in zone ZII based on splitting and color labeling. *Left cube*: 3D-reconstruction of microstructure in zone ZII from FIB-tomography with nickel (gray), CGO (white) and pores (black). *2nd cube from left* ($k = 0.0$), *2nd cube from right* ($k = 0.6$) and *right cube* ($k = 1.0$) represent the color labeled pore structures after splitting with increasing k-values. The corresponding PSD curves are shown in Fig. 9.

recently used for the time resolved characterization of nickel grain growth in SOFC anodes exposed to dry and humid gas at 950 °C [24].

3.1.4. Triple phase boundary length (TPB_L), specific surface area (SSA) and specific interface area (SIA): microstructural areas with electrochemical and with catalytic activity

In composite electrodes the triple phase boundary (TPB) represents the microstructural area where electrochemical reactions take place [15,20,31,35]. However the oxidation of fuel involves numerous reaction steps and many of those are not strictly bound to the TPB location [32,36]. For example adsorption and dissociation of hydrogen takes place on the nickel surface which is known for good catalytic properties. Thereby, not the entire nickel surface but only its interface with the pores is exposed to the gas phase and can therefore react with the fuel. In order to elaborate the microstructural effects on the electrochemical reaction steps it is thus important to be able to quantify the triple phase boundary length (TPB_L) and the specific surface areas (SSA) of each phase. In addition for each surface it should be distinguished between the different interfaces with the neighbouring phases. These parameters can be extracted both from 3D data (e.g. FIB-tomography) and from 2D images (e.g. SEM/BSE). However, as mentioned earlier, the distinction between active and total TPB_L can only be determined in 3D.

Fig. 12a shows a sub-volume of the 3D microstructure in zone ZII of the composite Ni/CGO anode. Already from this qualitative visualization it becomes obvious that the nickel phase is much coarser than the CGO and pore phases. Consequently, it can be expected that the coarse nickel phase has a lower specific surface area than the finer CGO and pore phases. From the segmented FIB-data the surfaces can be reconstructed by triangulation of the 3D phase boundaries. The corresponding specific surface areas are then measured and shown as a pie-diagram in Fig. 12b. As expected, the pore and CGO phases have much higher surface areas than nickel (0.3 and 0.26 vs. 0.13 $\mu m^2\ \mu m^{-3}$). From a point of view of the electrochemical activity it would be thus beneficial to reduce the particle size of nickel.

In the pie-diagram (Fig. 12b) the specific interface areas (ISA) are indicated between the areas representing the surfaces of each phase. For example the surface area of the nickel phase ($0.13\ \mu m^{-1}$) is divided into the interfaces nickel–pore ($0.45\ \mu m^{-1}$) and nickel–CGO ($0.85\ \mu m^{-1}$). Thus, only 35% of the total nickel surface in zone ZII is exposed to the pore phase and can be used for surface catalytic reactions with the gaseous fuel. The total TPB_L

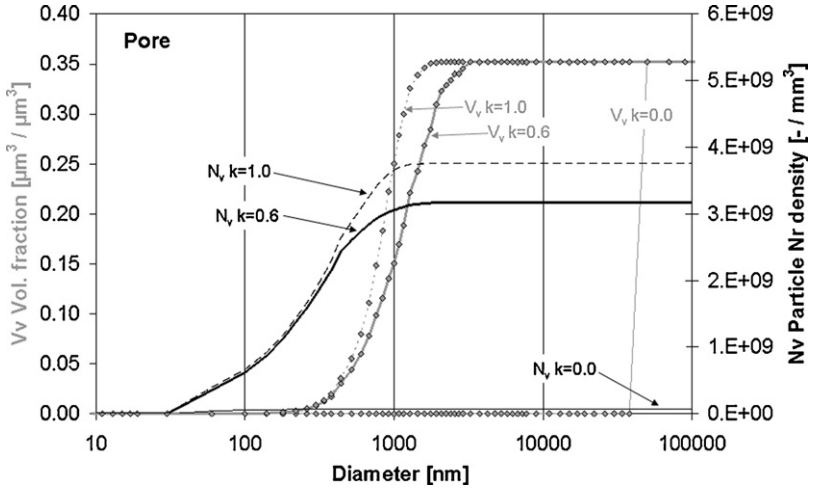

Fig. 9. Cumulative size distribution curves (PSD_D) of discrete pore objects in zone ZII, before splitting ($k = 0$), after 'realistic' splitting ($k = 0.6$) and with maximum splitting ($k = 1.0$). Vv denotes cumulative PSD curves related to the volume fraction. Nv denotes the cumulative PSDs related to the particle number density.

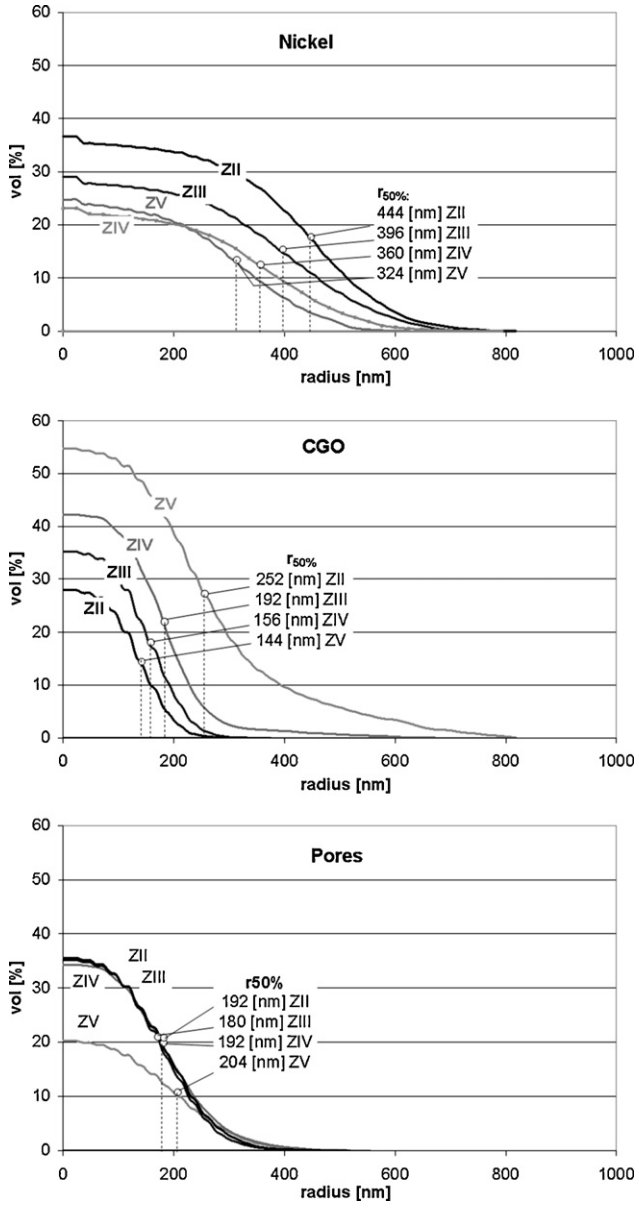

Fig. 10. Continuous PSD_C of nickel (top), CGO (middle) and pores (bottom) for all four zones (ZII to ZV) in the graded anode microstructure. The decreasing volume fractions of nickel from zone ZII to zone ZV are associated with a gradual decrease of the particle sizes (r_{50} = radius at 50% of the maximum cumulative volume). In a similar way, also the volume fractions and the particle sizes of CGO are increasing gradually from ZII to ZV. In contrast, the pore volume and pore size distributions are nearly identical in the zones ZII, ZIII and ZIV. In zone ZV the pore volume is reduced, but the average pore size is slightly larger compared to the other three zones.

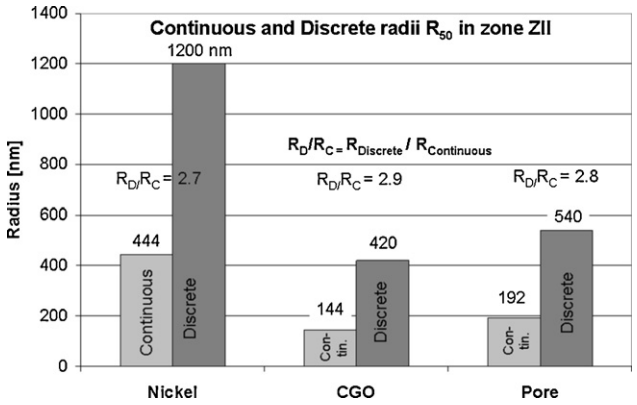

Fig. 11. Comparison of 'average radii' R_{50} from discrete and continuous PSDs measured for nickel, CGO and pores in zone ZII. Note that discrete and continuous PSDs are based on different geometrical concepts which lead to different results in the size measurements. These different geometrical concepts are illustrated above in Fig. 1. *Note*: The ratio of R_{50} radii from discrete and from continuous methods (R_D/R_C) is nearly identical for all three phases (i.e. 2.8 ± 0.1). This value of 2.8 can thus be considered as a proportionality factor between discrete and continuous measurements of R_{50} radii.

in zone ZII is 2.6 μm^{-2} which is in agreement with the range of most reported TPB_L values between 1 and 10 μm^{-2} [2,8,31]. As shown previously the percolation of nickel, CGO and pore phases in ZII is nearly 100% and hence the total TPB_L is electrochemically active, which is different from other FIB-tomography studies where a reduction of the TPB activity by 11% [8], 32% [7] and 40 to 60% [10] were determined due to isolated non-percolating particles in the investigated anode microstructure.

The TPB_L is certainly depending on the overall anode composition and on the grain sizes of each component. However, a change in volume fraction of a certain phase (e.g. nickel) is always coupled with a relative change of the other phases (e.g. pore and CGO). In addition the average grain sizes are also coupled with the corresponding volume fractions as shown in Fig. 10. Therefore the impact of compositional changes on the TPB_L is difficult to predict and so far hardly any systematic experimental investigation was presented on this issue.

Fig. 13 illustrates the TPB_L as a function of the graded anode compositions in zones ZII to ZV. The TPB_L gradually decreases from ZII to ZV. In Fig. 13(left) a negative correlation is documented for the TPB_L with the CGO contents and a positive correlation with nickel and pore contents. Apparently, the TPB_L is not linearly correlated to the surface area of any specific phase (Fig. 13 right). Especially the surface area of the CGO phase changes in a very different way than the TPB_L. In summary, the observed gradual change of the TPB_L appears to be a result of the overall compositional changes. However, it seems that changes in volume fraction and surface area of the coarsest phase (nickel) have a stronger impact on the TPB_L than the changes of the finer grained phase (CGO).

In this context also qualitative microstructural observations are important for the interpretation. It was observed in a previous study on anode degradation [24] that CGO 'surface wetting' leads to the formation of thin CGO layers which tend to cover the nickel grains. It was also reported that this effect increases with higher CGO contents. The increasing formation of CGO surface layers with increasing surface content may lead to a decrease of the TPB_L. This could explain the negative correlation between increasing CGO contents and decreasing TPB_L in zones ZII to ZV (Fig. 13 left).

In Fig. 14 the gradual change of the TPB_L in zones ZII to ZV is also compared with the corresponding specific interface areas (SIA). Thereby a significant correlation is observed between the TPB_L with the interface area between nickel and pore. Since this is the smallest interface area it seems to be the limiting microstructural factor for the TPB_L formation.

For the electrochemical activity of the investigated anode the interface between nickel and pore seems to be a crucial microstructural feature, since it is not only representing the catalytically active surface, but it also represents the limiting factor for the formation of the TPB_L. The pore–nickel interface is negatively correlated with the volume fraction of CGO because at higher CGO contents a continuous ceramic layer is formed on the surface of the nickel grains.

In summary the investigated Ni/CGO anode has a graduated microstructure in order to optimize transport properties and electrochemical activity according to the functionality of the different zones (i.e. gas distribution and current collection in ZII, electro-

chemical activity in ZV). Perfect percolation of all three phases is observed which provides good transport properties for gases in the pores and for charge carriers in the solid phases. However, in the functional anode layer (ZV) the microstructure is not really ideal. In this zone the highest electrochemical activity is expected. However, the decrease of the TPB_L and of the interface area between pore and nickel phases from zone ZII to ZV may negatively affect the electrochemical activity of the functional anode layer close to the electrode interface (ZV).

In this context it also has to be mentioned that CGO is a mixed electronic–ionic conductor under reducing conditions. Therefore the electrochemical activity is not strictly limited to the TPB (in contrast to Ni/YSZ anodes). However, for the discussion of purely geometrical aspects in the present paper these electrochemical issues are neglected.

3.2. Anode degradation in humidified forming gas at 950 °C: correlation between nickel coarsening and decrease of TPB_L and surface area (SSA, ISA)

In the previous section it was shown that the amount of electrochemically active sites (i.e. the TPB_L) is strongly correlated with the amount of the catalytically active surface area (i.e. the pore–nickel interface). During service life the cermet anodes undergo microstructural degradation whereby grain growth of nickel is a prominent feature. The question thus arises in which way the TPB_L and the pore–nickel interfaces are affected by the microstructural degradation in general and by the nickel grain growth in particular.

The microstructural degradation of nickel/CGO anodes was investigated for dry and for humid gas compositions at 950 °C in

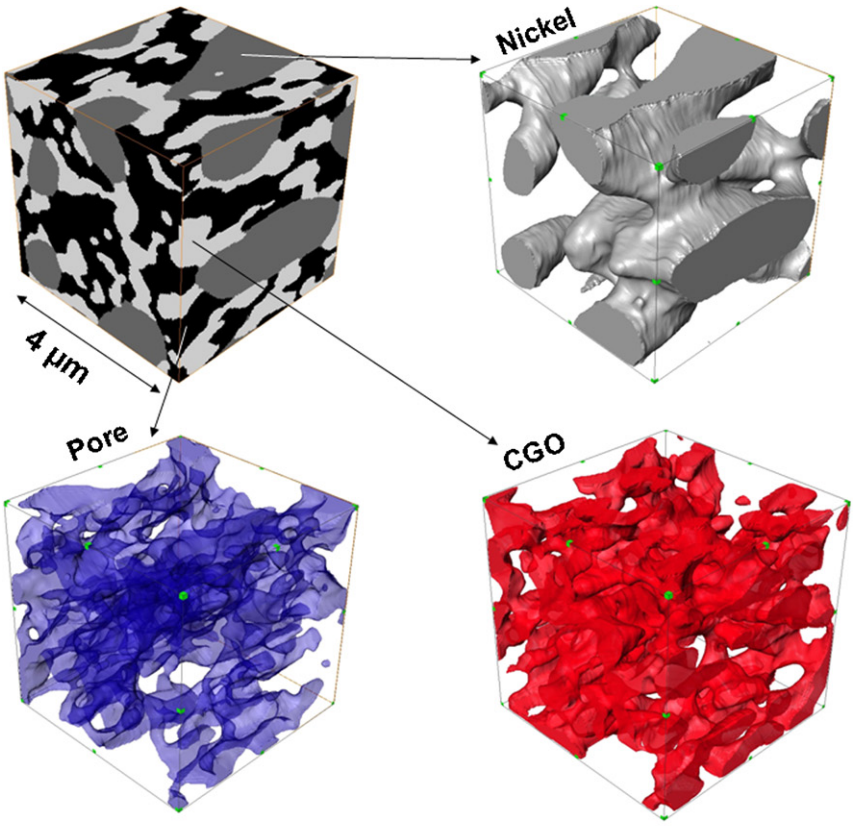

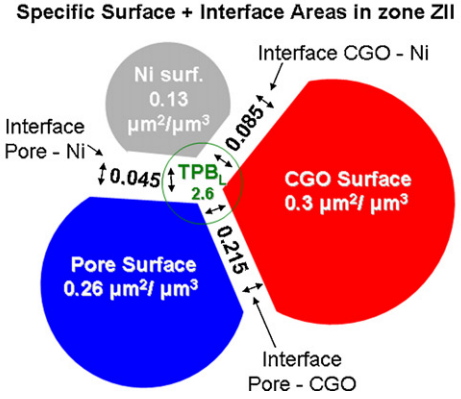

Fig. 12. (a) 3D-reconstruction of the surfaces in a small cube from zone ZII of Ni/CGO anode. The corresponding specific surface areas (SSA) and interfaces (SIA) are shown in b. (b) Pie-diagram representing the specific surface areas (SSA) of Ni, CGO and pores and the specific interface areas (SIA) between the three neighbouring phases of zone ZII. The sum of all interfaces is equal to the sum of all surfaces. The triple phase boundary length (TPB_L) is 2.6 µm µm^{-3}. *Note*: Only 35% of the nickel surface is exposed to the gas phase (pore–nickel interface), which represents the surface fraction with catalytic activity.

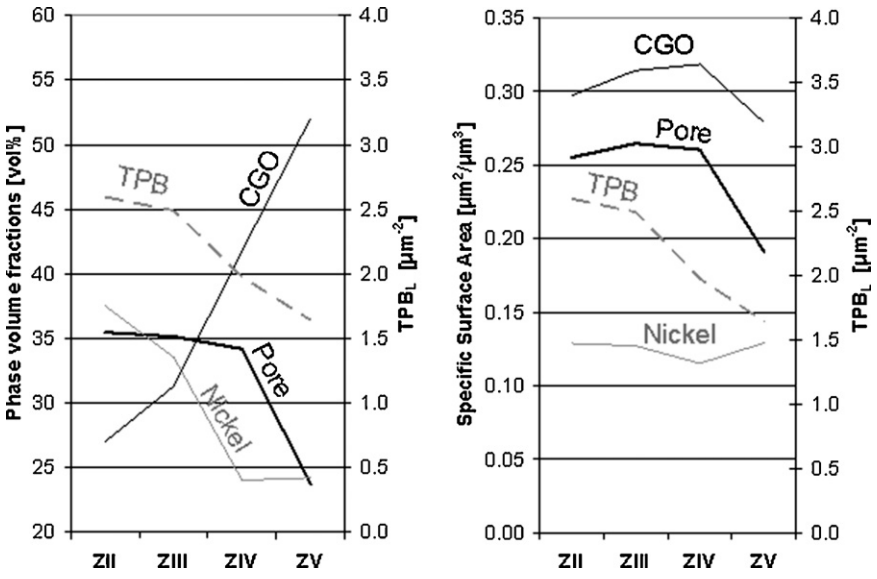

Fig. 13. Comparison of triple phase boundary length (TPB_L) with the phase volume fractions (left) and with specific surface areas (right) of nickel, CGO and pores in zones ZII to ZV of a composite anode. *Left*: The TPB_L strongly correlates with the volume fraction of nickel (and pore), but it is largely independent from the CGO content. *Right*: The TPB_L does not correlate well with the surface area of any specific phase.

previous studies [23,24]. Thereby, grain growth of nickel was the main microstructural feature under investigation. In the present paper we have extended this investigation on anode degradation by measuring the corresponding TPB_L and surface/interface analyses from the same samples and the same image data.

The findings from the previous study are briefly summarized in Figs. 15 and 16. As illustrated qualitatively in Fig. 15 the grain growth of nickel is relatively fast during the initial period (approximately 200 h). At long exposure times (>1000 h) the growth kinetics is reduced and the size of the nickel grains does not increase markedly. However the formation of CGO layers on the nickel surfaces becomes a prominent feature, especially for anode layer 2 (see ZII in Fig. 15c).

The quantitative evolution of the nickel grain sizes (R_{50}) in anode layers 1 and 2 are shown in Fig. 16 modified after [23,24]. The data illustrates that growth rates are very high during the initial period (<200 h) and become nearly zero for exposure times longer than 1000 h. The compositional analyses (not shown here, see [24]) indicate that nickel contents decrease slightly at long exposure times, which was interpreted as evidence for nickel evaporation due to the formation of volatile nickel hydroxide species. Correspondingly the CGO content is passively enriched (relative to the nickel). This increase of CGO leads to the formation of surface layers on the nickel grains. This effect is particularly strong in anode layer 2 after 2286 h (ZII in Fig. 15c).

In the previous section it was discussed that the formation of a CGO surface layer may lead to a reduction of the TPB_L and of the pore–nickel interface. The decreasing TPB_L due to the formation of CGO surface layers may thus negatively affect the electrochemical electrode performance. However, in the context with the ongoing microstructural degradation the CGO surface layers may also have a positive effect on electrode durability since these layers

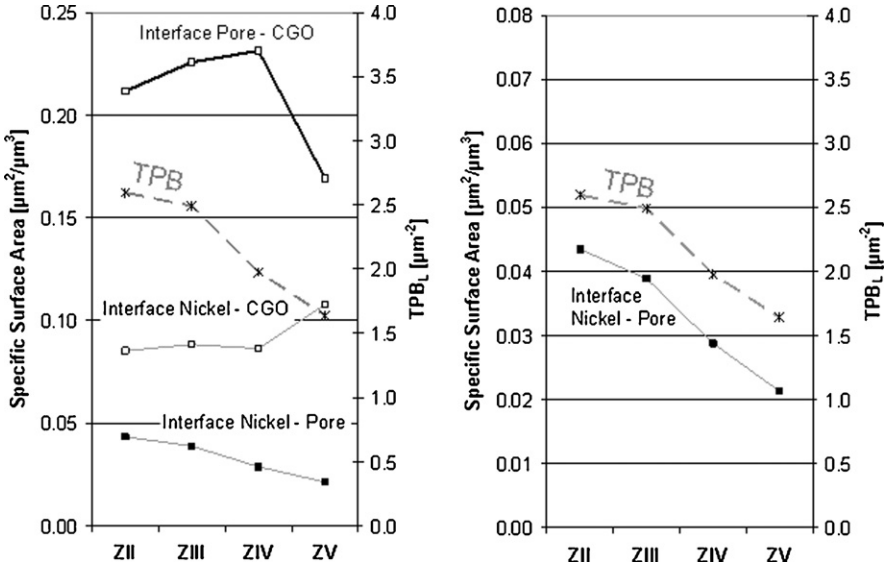

Fig. 14. Comparison of triple phase boundary length (TPB_L) with the specific interface areas in zones ZII to ZV of a composite Ni/CGO anode. The gradual change of the TPB_L correlates nicely with the changes of the specific interface area (SIA) between nickel and pore. This correlation becomes more obvious when adjusting the scales (Fig. 14, right side).

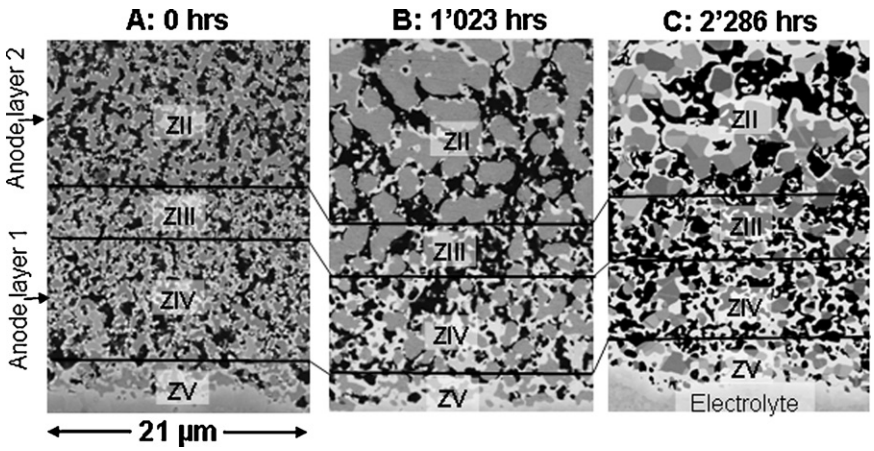

Fig. 15. SEM images of porous nickel/CGO anodes which were exposed to a humidified forming gas at 950 °C, modified after [24]. Significant nickel coarsening occurs during exposure between 0 h (left) and 1023 h (middle). Between 1023 h (middle) and 2286 h (right) the nickel particle sizes remain stable. The images are analyzed for quantification of continuous PSD_C (see Fig. 16), of surface and interface areas (SSA, SIA) and of triple phase boundary length (TPB_L) (see Fig. 17). *Note*: Anode layer 1 and anode layer 2 correspond to zones ZIV and ZII in the previous sections (e.g. in Fig. 2).

protect the nickel grains from further mobilization (see discussion in [24]).

The evolution of the total TPB_L and the corresponding nickel surfaces in the same samples that were exposed to a humidified forming gas at 950 °C are shown in Fig. 17. The synchronous evolution of these parameters (total TPB_L, SSA, and ISA) is remarkable and confirms the previous conclusions that TPB_L and the pore–nickel interface are strongly correlated (see Fig. 14). Furthermore the comparison of Fig. 16 and Fig. 17 also indicates that the fast decrease of TPB_L during the initial period is associated with the growth kinetics of nickel at the same time. At longer exposure time, when nickel grain size is stable (see Fig. 16), the TPB_L and the nickel surfaces and interfaces are still decreasing. The degradation during long time exposure is thus not related to further grain growth of nickel. As mentioned above, there is evidence for volatilization of nickel which also leads to the formation of CGO layers on the nickel surface and to a reduction of the total TPB_L and of nickel surface/interface areas. Apparently these are the dominating anode degradation features at long time exposure in a humidified gas environment.

It is important to note, that the data from the degradation experiments (Fig. 17) are based on 2D analyses and therefore only the total TPB_L is measured. The effect of isolated particles (nickel or CGO) which are not connected with the main network of the corresponding phase cannot be quantified in 2D. The measured total TPB_L values thus represent a maximum estimation of the active TPB_L. It must be assumed that nickel coarsening and formation of CGO layers may lead to a loss of percolation (mainly of the nickel phase) during the ongoing degradation. It is thus likely that the decrease of the active TPB_L due to microstructural degradation is even larger than the measured loss of the total TPB_L which is documented in Figs. 17 and 18.

3.3. Comparison of microstructures in real samples (this study) and in virtual models (from literature)

As noted in the introduction various studies dealing with microstructural modeling indicate that there is a strong interdependency of the TPB_L with the particle sizes as well as with the compositions of composite anodes [18–20,33]. Some results from literature are shown in Fig. 18, which illustrates the changes of the TPB_L with the nickel content (note the following relationship for the solid volume fractions of electronic (Ni) and ionic (CGO or YSZ) conducting phases: $\Phi_{el} + \Phi_{ion} = 1$). The lines nr 1 [20] and nr 2 [19] in Fig. 18 both give symmetric curves because the average sizes of

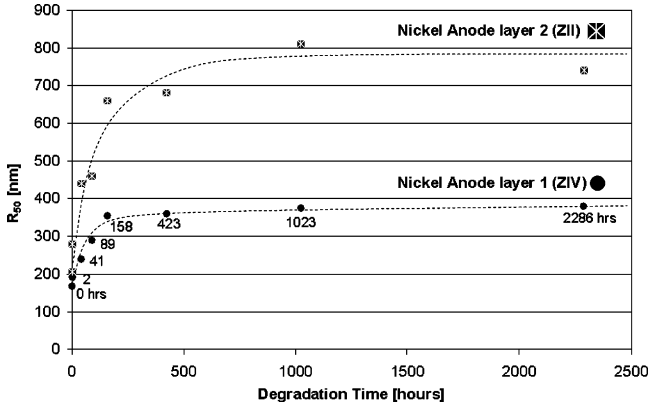

Fig. 16. Evolution of nickel grain growth ('average radius': R_{50}) during exposure to a humidified forming gas at 950 °C. During the initial phase (first 200 h) rapid grain growth occurs. At longer exposure time the nickel grain size remains stable. The R_{50} values for each time step are representing the average from 5 different continuous PSD_C measurements in order to guarantee representative analyses (data modified after [23,24]).

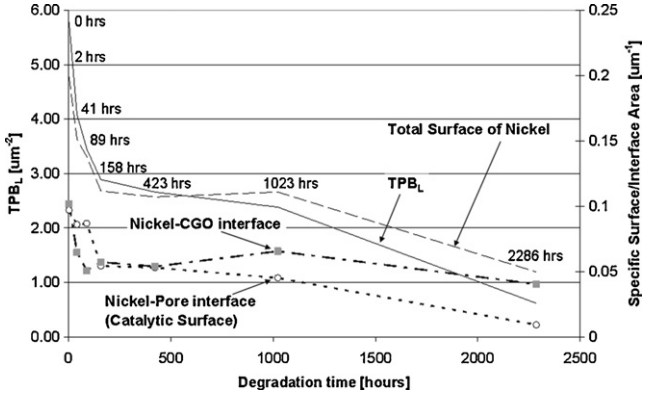

Fig. 17. Evolution of TPB_L and specific interface areas (SIA) of nickel during exposure to a humidified forming gas at 950 °C for up to 2286 h. There is a strong correlation between the TPB_L and the pore–nickel interfaces as well as with the entire nickel surface area. During the initial phase (first 200 h) the TPB_L and the pore–nickel interfaces rapidly decrease which is contemporaneous with the fast grain growth of nickel (see Fig. 16). At longer exposure time the TPB_L and nickel interfaces decrease slowly but constantly whereas during this period no further nickel grain growth is observed (compare with Figs. 15 and 16).

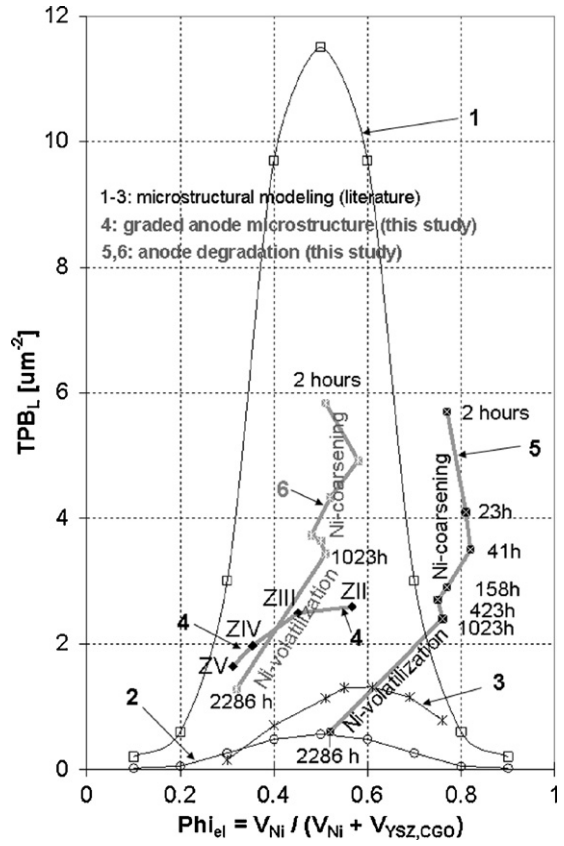

Fig. 18. Comparison of triple phase boundary length (TPB_L) from microstructural modeling (virtual geometries) and from quantitative analyses of real composite anodes (this study). The TPB_L are plotted vs. the nickel contents which is the solid volume fraction of the electronic conducting phase ($\Phi_{el} = V_{el}/(V_{el} + V_{ion})$). The results from microstructural modeling (data points 1–3) indicate that TPB_L is strongly depending on the particle size. Data point 3 shows that for the case where the electronic conductor is coarser than the ionic (YSZ), maximum TPB_L is reached at composition of $\Phi_{el} = 0.6$. More detailed information is given in Table 1.

nickel and YSZ are equal ($r_{el}/r_{ion} = 1.0$). For this symmetric case the maximum TPB_L is obtained when $\Phi_{el} = \Phi_{ion} = 0.5$. However since the particle size in nr 1 is much finer ($r_{el} = r_{ion} = 250$ nm) than in nr 2 ($r_{el} = r_{ion} = 1000$ nm) this results in much higher TPB_L (and higher surface areas). For line nr 3 the particle sizes of nickel and YSZ are not equal ($r_{el} = 1000$ nm/$r_{ion} = 500$ nm) and therefore an asymmetric curve is obtained. For this case the maximum TPB_L is shifted to compositions of $\Phi_{el} = 0.6$. The maximum TPB_L is thus obtained when the amount of the coarser phase is larger than the finer.

The results from modeling are compatible with our findings from real microstructures. In the graded anode microstructure (curve nr 4) the nickel contents are gradually increasing from zone ZV ($\Phi_{el} = 0.31$) to ZII ($\Phi_{el} = 0.57$) where a maximum TPB_L of 2.6 μm^{-2} is reached. In contrast to the microstructural modeling the particle sizes are not independent from the volume fractions and hence the graded composition also induces gradual changes of the particle sizes. Thereby the grain size of nickel is increasing towards ZII whereas CGO is coarsening towards ZV. This example illustrates that in real materials the microstructural parameters cannot be changed independently from each other. This fact restricts the practical possibilities of a microstructural optimization in real samples.

The curves number 5 (anode layer 1) and 6 (anode layer 2) represent the changes of TPB_L during microstructural degradation in a humidified forming gas at 950 °C (compare Figs. 15–18). During the first 200 h grain growth of nickel leads to a rapid decrease of the TPB_L. The reduction of TPB_L is more severe for anode layer 2 which has a higher amount of nickel. Between 158 and 1023 h the TPB_L is changing only slightly. At longer exposure times up to 2286 h the reduction of TPB_L is associated with the volatilization of nickel [24]. Overall this processes and the kinetics of TPB-reduction seem to be similar in both anode layers.

Overall the results from microstructural modeling and from quantitative analysis of real microstructures give compatible results. However, it has to be noted that the active TPB_L resulting from the microstructural modeling is strongly affected by depercolation phenomena which become very prominent close to the theoretical percolation thresholds ($\Phi_{el} \leq 0.3$ and $\Phi_{el} \geq 0.6$). From the present study the importance of depercolation in real anode microstructures cannot be observed in a similar way. First of all, the compositions analyzed here are all well within the theoretical percolation thresholds ($\Phi_{el} = 0.31$–0.57). In addition the real microstructures are less 'rigid' in the sense that the phase with the smaller particle size (i.e. CGO) forms a fine structured continuous network between the coarse nickel grains. The more fine grained structures are thus not randomly distributed as it is usually the case for rigid particles in computational modeling. The real structures after sintering thus seem to have much better connectivity than what is predicted from the modeling with spherical particles. The main difference between the real microstructures compared to the ideal, virtually created geometries are the more complex particle shapes, the wider particle size distributions and the non-random spatial distributions of the finer particles (e.g. due to the wetting of nickel surfaces by thin CGO layers). This leads to a better percolation and higher activity of the triple phase boundaries in real samples (at least for the anode material of the present study).

4. Conclusions

The triple phase boundary length (TPB_L) and the pore–nickel interfaces represent the microstructural sites which strongly affect the electrochemical kinetics and the catalytic activity in the composite anodes. The effects of composition and of particle size distributions on the TPB_L and on the various types of surfaces and interfaces have been investigated quantitatively by means of FIB-nanotomography and with dedicated image analysis tools. For this purpose an anode with a graded microstructure (four distinct zones with gradually changing compositions) was investigated and the results compared with microstructural modeling from literature.

After sintering the cermet phases are forming continuously percolating networks and therefore the initial grain boundaries are difficult to identify. Reliable object recognition is thus a major challenge for the analysis of discrete particle size distributions (PSD_D). For this purpose a splitting procedure was introduced [26]. This method however can only be performed based on 3D-reconstructions of the anode microstructure, e.g. from FIB-nanotomography which limits the number of investigated samples. The splitting with a *k*-value of 0.6 leads to realistic particle structures [27]. These discrete particle structures are the basis for a quantitative validation of the virtual particle structures that are produced by microstructural modeling (e.g. [19,20]).

An alternative method for particle size determination is the continuous PSD_C which can be applied to networked microstructures without preceding recognition of the discrete particles. In addition the continuous PSD_C method is also proven to give reliable result based on 2D images [30]. Compared to the discrete PSD the continuous method is more reliable when the particle shapes are very complex, because this causes problems for reliable object recognition. The present study reveals a constant ratio between continuous and discrete PSDs that can be described with a proportionality factor of 2.8.

The total TPB_L as well as the surface and interface areas can be determined from 2D and from 3D images. For realistic microstructures there is no simple correlation between the TPB_L with composition and particle size. However, the study of the 4 different zones indicates that the TPB_L correlates with the volume fractions of the coarsest phase (i.e. nickel). Even more pronounced is the correlation between the TPB_L with the pore–nickel interface. Because this is the least abundant surface in the microstructure it represents the limiting parameter for the TPB formation.

Upon exposure to a humid gas at 950 °C, rapid nickel grain growth is observed for the initial period (<200 h). This coarsening leads to a strong reduction of the nickel surfaces (including pore–nickel interface) and of the associated TPB_L. At longer exposure times grain growth ceases but nickel volatilization leads to the formation of thin CGO layers on the surface of the nickel grains. Thereby the pore–nickel interface and also the TPB_L are strongly reduced.

Overall, the comparison of real anode structures with computational models reveals similar trends how the TPB_L changes with composition and pore size. However, wide particle size distributions, non-random spatial distributions and non-spherical particle shapes represent major problems for the computational simulation. In particular this study indicates different perceptions of the percolation threshold. A perfect percolation of all three phases (>99%) is observed in the real composite anode whereas depercolation in modeling studies is always a limiting factor for TPB_L-activity. These different findings question the practical value of the percolation theory based on idealized microstructures. The mentioned disordering due to wider particle size distributions and the more complex particle shapes may be a reason for the higher degree of percolation that is observed in the present study for real microstructures. The investigation of percolation and connectivity is important for the understanding of the relationship between microstructure, electrode activity and transport properties. This issue is thus currently the focus of more rigorous investigations at empa by means of FIB-tomography and by network analysis of skeleton graphs.

Acknowledgements

The research presented in this paper was performed within the framework of a Swiss national project (SFOE project no. 102290: SOF-CH) and an ERA-NET project (SFOE project no. 102746: AccelenT). Financial support by the Swiss Federal Office of Energy (SFOE) and by Swisselectric Research is gratefully acknowledged.

References

[1] R.J. Gorte, J.M. Vohs, Current Opinion in Colloidal and Interface Science 14 (2009) 236–244.
[2] N. Shikazono, D. Kanno, K. Matsuzaki, H. Teshima, S. Sumino, N. Kasagi, Journal of the Electrochemical Society 157 (2010) B665–B672.
[3] A.V. Virkar, J. Chen, C.W. Tanner, J.W. Kim, Solid State Ionics 131 (2000) 189–198.
[4] L. Holzer, F. Indutnyi, P. Gasser, B. Münch, M. Wegmann, Journal of Microscopy 216 (2004) 84–95.
[5] L. Holzer, M. Cantoni, in: P. Russell, I. Utke, S. Moshkalev (Eds.), Nanofabrication with Focused Electron and Focused Ion Beam, Oxford University Press, in press.
[6] M.D. Uchic, L. Holzer, B.J. Inkson, E.L. Principe, P. Munroe, MRS Bulletin 32 (2007) 408–416.
[7] J.R. Wilson, A.T. Duong, M. Gameiro, H.Y. Chen, K. Thronton, D.R. Mumm, S.A. Barnett, Electrochemical Communications 11 (2009) 1052–1056.
[8] J.R. Wilson, M. Gameiro, K. Mischaikow, W. Kalies, P.W. Voorhees, S.A. Barnett, Microscopy and Microanalysis 15 (2009) 71–77.
[9] J.R. Wilson, W. Kobsiriphat, R. Mendoza, H.-Y. Chen, J.M. Hiller, D.J. Miller, K. Thornton, P.W. Voorhees, S.B. Adler, S.A. Barnett, Nature Materials 5 (2006) 541–544.
[10] H. Iwai, N. Shikazono, T. Matsui, H. Teshima, M. Kishimoto, R. Kishida, D. Hayashi, K. Matsuzaki, D. Kanno, M. Saito, H. Muroyama, K. Eguchi, N. Kasagi, H. Yoshida, Journal of Power Sources 195 (2010) 955–961.
[11] P.R. Shearing, J. Golbert, R.J. Chater, N.P. Brandon, Chemical Engineering Science 64 (2009) 3928–3933.
[12] D. Gostovic, J.R. Smith, D.P. Kundinger, K.S. Jones, E.D. Wachsman, Electrochemical and Solid State Letters 10 (2007) B214–B217.
[13] D. Gostovic, N.J. Vito, K.A. O'Hara, K.S. Jones, E.D. Wachsman, Journal of the American Ceramic Society, in press.
[14] K.N. Grew, Y.S. Chu, J. Yi, A.A. Peracchio, J.R. Izzo, Y. Hwu, F. De Carlo, W.K.S. Chiu, Journal of the Electrochemical Society 157 (2010) B783–B792.
[15] A. Bieberle, L.P. Meier, L. Gauckler, Journal of the Electrochemical Society 148 (2001) A646–A656.
[16] M.E. Lynch, D.S. Mebane, Y. Liu, M. Liu, Journal of the Electrochemical Society 155 (2008) B635–B643.
[17] M. Vogler, A. Bieberle-Hütter, L. Gauckler, J. Warnatz, W.G. Bessler, Journal of the Electrochemical Society 156 (2009) B663–B672.
[18] A. Abbaspour, J.-L. Luo, K. Nandakumar, Electrochimica Acta 55 (2010) 3944–3950.
[19] A. Abbaspour, X. Wen, K. Nandakumar, J. Luo, K.T. Chuang, Journal of Power Sources 185 (2008) 961–966.
[20] B. Kenney, M. Valdmanis, C. Baker, J.G. Pharoah, K. Karan, Journal of Power Sources 189 (2009) 1051–1059.
[21] A. Martinez, J. Brouwer, Electrochimica Acta 53 (2008) 3597–3609.
[22] A.M. Gokhale, S. Zhang, M. Liu, Journal of Power Sources 194 (2009) 303–312.
[23] B. Iwanschitz, A. Mai, L. Holzer, T. Hocker, M. Schütze, in: J.T.S. Irvine (Ed.), 9th European Solid Oxide Fuel Cell Forum, EFCF, Oberrohrdorf (CH), Luzern, 2010.
[24] L. Holzer, B. Iwanschitz, T. Hocker, B. Münch, M. Prestat, D. Wiedenmann, U. Vogt, P. Holtappels, J. Sfeir, A. Mai, T. Graule, Journal of Power Sources, in press, doi:10.1016/j.jpowsour.2010.08.017.
[25] M. Cantoni, C. Genoud, C. Hébert, G. Knott, Microscopy and Analysis 05/06 (2010) 13–16.
[26] B. Münch, P. Gasser, R. Flatt, L. Holzer, Journal of the American Ceramic Society 89 (2006) 2586–2595.
[27] L. Holzer, B. Münch, Microscopy and Microanalysis 15 (2009) 130–146.
[28] L. Holzer, B. Münch, M. Wegmann, R. Flatt, P. Gasser, Journal of the American Ceramic Society 89 (2006) 2577–2585.
[29] B. Münch, L. Holzer, J. Am. Ceram. Soc. 91 (2008) 4059–4067.
[30] L. Holzer, B. Muench, M. Rizzi, R. Wepf, P. Marschall, Applied Clay Science 47 (2010) 330–342.
[31] A. Faes, A. Hessler-Wyser, D. Presvytes, C.G. Vayenas, J. Van Herle, Fuel Cells 6 (2009) 841–851.
[32] W.G. Bessler, J. Warnatz, D.G. Goodwin, Solid State Ionics 177 (2007) 3371–3383.
[33] A. Ioselevich, A.A. Kornyshev, W. Lehnert, Solid State Ionics 124 (1999) 221–237.
[34] E. Underwood, Quantitative Stereology, Addison-Wesley Publishing, Menlo Park, 1970.
[35] D.G. Goodwin, H. Zhu, A.M. Colclasure, R.J. Kee, J. Electrochem. Soc. 156 (2009) B1004–B1021.
[36] H. Zhu, R.J. Kee, J. Electrochem. Soc. 155 (2008) B715–B729.